Reaction dynamics for the system ^{17}F + ^{58}Ni at near-barrier energies

M. Mazzocco,[1,2,*] C. Signorini,[1,2] D. Pierroutsakou,[3] T. Glodariu,[4] A. Boiano,[3] C. Boiano,[5] F. Farinon,[6] P. Figuera,[7]
D. Filipescu,[4] L. Fortunato,[1,2,8] A. Guglielmetti,[5,9] G. Inglima,[3,10] M. La Commara,[3,10] M. Lattuada,[7,11] P. Lotti,[2]
C. Mazzocchi,[5,9] P. Molini,[1,2] A. Musumarra,[7,12] A. Pakou,[13] C. Parascandolo,[3,10] N. Patronis,[13] M. Romoli,[3]
M. Sandoli,[3,10] V. Scuderi,[7,11] F. Soramel,[1,2] L. Stroe,[4] D. Torresi,[7,11] E. Vardaci,[3,10] and A. Vitturi[1,2]

[1]*Dipartimento di Fisica, Università di Padova, via F. Marzolo 8, I-35131 Padova, Italy*
[2]*Istituto Nazionale di Fisica Nucleare-Sezione di Padova, via F. Marzolo 8, I-35131 Padova, Italy*
[3]*Istituto Nazionale di Fisica Nucleare-Sezione di Napoli, via Cinthia, I-80126 Napoli, Italy*
[4]*National Institute for Physics and Nuclear Engineering (NIPNE), 407 Atomistilor Street, R-077125 Magurele, Romania*
[5]*Istituto Nazionale di Fisica Nucleare-Sezione di Milano, via Celoria 16, I-20133 Milano, Italy*
[6]*GSI Helmholtzzentrum für Schwerionenforschung, Planckstrasse 1, D-64291 Darmstadt, Germany*
[7]*Istituto Nazionale di Fisica Nucleare-Laboratori Nazionali del Sud (LNS), via Santa Sofia 62, I-95125 Catania, Italy*
[8]*ECT*, Strade delle Tabarelle 286, I-38123 Villazzano (TN), Italy*
[9]*Università degli Studi di Milano, via Celoria 16, I-20133 Milano, Italy*
[10]*Dipartimento di Scienze Fisiche, Università di Napoli, via Cinthia, I-80126 Napoli, Italy*
[11]*Dipartimento di Fisica ed Astronomia, Università di Catania, via Santa Sofia 64, I-95125 Catania, Italy*
[12]*Dipartimento di Metodologie Fisiche e Chimiche per l'Ingegneria, Università di Catania, I-95125 Catania, Italy*
[13]*Department of Physics, University of Ioannina and HINP, GR-45110 Ioannina, Greece*

Charged reaction products originated from the interaction of the loosely bound radioactive ion beam ^{17}F ($S_p = 600$ keV) with the proton-shell closed ^{58}Ni target were measured at two colliding energies slightly above the Coulomb barrier. The collected data were analyzed within the framework of the optical model to deduce the reaction cross section and to investigate the role played by inelastic excitations, transfer channels, and the breakup process ^{17}F $\rightarrow$ ^{16}O + p at near-barrier energies. The reaction cross section at the lower ^{17}F energy showed a moderate enhancement ($\sim$20%) with respect to that of the system ^{16}O + ^{58}Ni. At this energy direct reaction channels were also found to be more relevant than those for the reaction induced from the tightly bound projectile ^{16}O on the same target. Both features could be strongly related to the very low binding energy of the ^{17}F valence proton.

PACS number(s): 25.60.Bx, 25.60.Dz

I. INTRODUCTION

The reaction dynamics in collisions induced from light weakly bound nuclei has been one of the most studied and debated topics for the past 20 years at least. Some of these nuclei, called "halo" nuclei, have a radial extension much larger than that predicted from the systematics deduced for stable tightly bound nuclei close to the valley of β stability. This extended low-density nuclear matter distribution should, in principle, lead to a lowering of the Coulomb barrier in the case of a fusion process with a target nucleus, and therefore to an enhancement of the fusion probability. However, because these projectiles are generally very loosely bound ($S_{p,n,2n} < 1.0$ MeV), they can easily break into smaller fragments when they approach the strong Coulomb or nuclear field of a target nucleus. The interplay between halo structure effects and small binding energy gives rise to a rather peculiar scenario and the situation is particularly remarkable at colliding energies around the Coulomb barrier, where even for stable nuclei a large enhancement of the sub-barrier fusion cross section has been observed starting from the early 1980s [1]. The question of whether this enhancement could be even stronger with halo weakly bound nuclei has triggered many theoretical works and has stimulated a widespread experimental effort to deliver radioactive ion beams (RIBs) with high intensity and good energy resolution. Several review articles have been recently written on this topic [2–6].

Different approaches to this problem exist also from a theoretical point of view. Depending on whether the breakup channel is treated as an additional reaction channel or as removed flux from the incident beam, the fusion cross section is predicted to be enhanced or hindered with respect to the one-dimensional barrier penetration model. These two opposite views were somehow reconciled by Hagino *et al.* [7], who predicted that couplings to breakup (continuum) states lead to the enhancement of the complete fusion cross section at sub-barrier energies and to a reduction of the complete fusion cross section above the barrier. Hereafter we use the term "complete fusion" to indicate the fusion of the whole projectile with the target and the term "incomplete fusion" to refer to the process where only a projectile fragment fuses with the target. Finally, we define "total fusion" as the sum of complete and incomplete fusion.

Experiments performed to study the interaction of the most weakly bound stable nuclei, namely, ^{6}Li ($S_\alpha = 1.474$ MeV), ^{7}Li ($S_\alpha = 2.467$ MeV), and ^{9}Be ($S_n = 1.665$ MeV), with heavy targets (^{208}Pb and ^{209}Bi) [8] showed a fairly large

*marco.mazzocco@pd.infn.it

complete fusion suppression ($\sim$30%) at energies above the barrier and a moderate enhancement at sub-barrier energies. It was also found that for these systems the incomplete fusion accounted for the 30% reduction of the complete fusion cross section. Thus, no overall signature of breakup-related effects was measured for the total fusion. More recent data [9] on the above-barrier complete fusion cross section for the reactions induced from tightly bound boron isotopes, ^{10}B ($S_\alpha = 4.461$ MeV) and ^{11}B ($S_\alpha = 8.665$ MeV), on a ^{209}Bi target contributed to establishing a systematic variation of the complete fusion suppression as a function of the projectile breakup threshold energy.

Reactions induced by the most weakly bound stable projectiles, such as ^{9}Be + ^{208}Pb [10], ^{9}Be + ^{209}Bi [11], ^{6,7}Li + ^{28}Si [12,13], ^{6,7}Li + ^{208}Pb [14,15], and from radioactive ^{6}He nuclei ($S_\alpha = 0.972$ MeV) on ^{64}Zn [16], ^{63,65}Cu [17,18], ^{208}Pb [19], ^{209}Bi [20,21], and ^{238}U [22] targets evidenced fairly large α-particle production cross sections at energies around the Coulomb barrier. The origin of these α particles could be manifold: noncapture breakup, transfer channels, incomplete fusion, and evaporation after compound nucleus formation. Extensive studies performed for the system ^{6}He + ^{209}Bi showed that at secondary beam energies around 22.5–23.0 MeV, 20% of the total α-particle yield was attributable to the $1n$ transfer [23], 55% to the $2n$ transfer [24], and, finally, 25% to the noncapture breakup [25]. The relevance of direct transfer channels was also confirmed by other experiments performed with the ^{6}He radioactive beam [16–18] and with the stable weakly bound ^{6}Li projectile [13,26]. As a general feature, all these systems exhibited reaction cross sections larger than the total fusion cross sections, especially at sub-barrier energies. This outcome indicates that the small breakup threshold and the projectile halo structure mainly enhance the reaction cross section rather than the total fusion probability.

Within this framework, elastic scattering experiments provide basic information on the "reactivity" of an exotic projectile and considering the intensity of the presently available RIBs, still several orders of magnitude smaller than stable beams, this could be the only achievable information for some of these exotic nuclei. We therefore undertook the investigation of the system ^{17}F ($S_p = 0.600$ MeV) + ^{58}Ni at two energies slightly above the nominal Coulomb barrier ($V_{B,lab} \approx 46$ MeV). This study will provide complementary information with respect to that collected for the interaction of ^{17}F with the heavy target ^{208}Pb on fusion [27], elastic scattering, and breakup [28–31]. A first report on the present experiment was presented at the 10th International Conference on Nucleus-Nucleus Collisions (NN2009) [32].

The article is organized as follows: Section II will describe the radioactive beam production technique. Section III will present the experimental setup and the data analysis. Section IV will show the optical model analysis of the collected data. The relevance of inelastic excitations, transfer channels, and the breakup process on the reaction dynamics is discussed in Sec. V together with a comparative analysis of the reaction cross-section data available for reactions induced from light weakly bound projectiles on medium-mass targets. Some concluding remarks are finally drawn in Sec. VI.
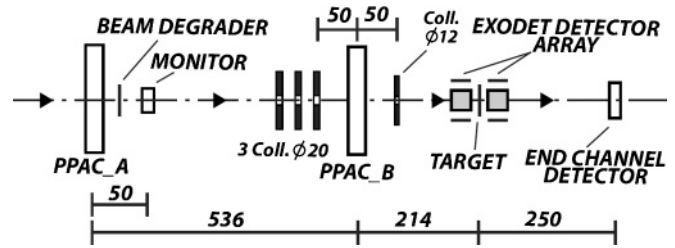

FIG. 1. Layout of the secondary beam tracking system and the beam diagnostic detectors of the facility EXOTIC. All dimensions are in millimeters.

II. SECONDARY BEAM PRODUCTION

A. The facility EXOTIC

The ^{17}F radioactive beam for this experiment was produced with the facility EXOTIC [33] at the Laboratori Nazionali di Legnaro (Italy) of the Istituto Nazionale di Fisica Nucleare. This facility was laid out for the production of light RIBs employing two-body reactions induced from a high-intensity heavy-ion beam delivered from the LNL-XTU Tandem Van de Graaff accelerator on a gas target. The gas cell is 5 cm long, double walled with 2.2-μm-thick Havar foils and can be filled with H_2, D_2, ^{3}He, and ^{4}He gases up to a pressure of 1 bar. The target station can operate at both room and liquid-nitrogen temperatures. The selection, separation, and focusing of the secondary beam are accomplished by a series of eight ion-optical elements [a first quadrupole triplet, a 30°-bending magnet, a 1-m-long Wien filter (WF), and a second quadrupole triplet] and four slit sets located at suitable positions along the beam line [34].

Two parallel plate avalanche counters (PPACs) have been recently located 750 and 214 mm upstream the secondary target to provide an event-by-event reconstruction of the position hit on the target (see Fig. 1 for a schematic layout of the secondary beam tracking system). Each PPAC consists of a cathode plate placed between two anodes. The anodes are made by 60 wires at a distance of 1.0 mm with their orientations perpendicular to each other, allowing a position resolution of 1.0×1.0 mm^2. The wires are connected to delay lines of 2.5 ns/mm, yielding a total delay time of 150 ns for the whole line. Signals are collected from each end of the delay lines in both the x and the y directions and from the cathode for a total amount of five signals for each PPAC. The space between the anode and each cathode is filled with isobutane (C_4H_{10}) gas at a pressure of 12 mbar. The detector windows are made from 1.5-μm mylar foils. The cathode is also a 1.5-μm mylar foil with 30 nm of aluminum evaporated on both surfaces.

The first PPAC, named PPAC_A, is placed in a small reaction chamber at the exit of the second quadrupole triplet. The second PPAC, called PPAC_B, is located at the entrance of the main reaction chamber. A mylar-aluminum degrader foil (not used in the present experiment) with suitable thickness could be inserted behind PPAC_A to decrease the secondary beam energy at the cost of a slightly worse energy resolution and an approximately 30% reduction in intensity. This operation could save the time needed to retune the primary accelerator and the whole facility EXOTIC to the new

energy to be delivered. Finally, a stack of three collimators with diameters of 20 mm is placed between the two PPACs ($\sim$264–324 mm upstream the secondary target) and a 12-mm collimator is located just behind PPAC_B ($\sim$164 mm upstream the secondary target; see Fig. 1).

B. Production reaction

In the present experiment we used a 100-MeV ^{17}O^{6+} primary beam with intensity around 100 pnA impinging on a H$_2$ gas target. The production reaction was ^{1}H(^{17}O,^{17}F)n ($Q_{\text{value}} = -3.54$ MeV). Two different ^{17}F secondary beam energies were obtained operating the target at different conditions. The former, 54.1 ± 1.1 MeV, was achieved with a gas pressure of 750 mbar at liquid-nitrogen temperature (corresponding to an equivalent thickness of $\sim$1 mg/cm^2). The latter, 58.5 ± 1.0 MeV, was obtained by increasing the gas pressure up to 950 mbar and warming up the target to room temperature (equivalent thickness, 0.38 mg/cm^2). In both cases the radioactive beam intensity was around 10^5 pps.

C. Secondary beam selection and purification

Figure 2 shows two energy spectra collected with a silicon detector (called "monitor" in Fig. 1; active area, 200 mm^2; thickness, 300 μm), which could be alternatively inserted along the beam axis 700 mm upstream the secondary target (i.e., just behind PPAC_A; see Fig. 1). The top spectrum was obtained at the lower secondary beam energy with the WF off. We can clearly distinguish three well-pronounced peaks related to the 6+, 7+, and 8+ charge states of the ^{17}O scattered beam and a small bump at around 60 MeV corresponding to the RIB under production. The bottom panel shows the same spectrum after applying a voltage difference of $\pm$40 kV across the electrodes of the WF. This value corresponds to 80% of

FIG. 3. Energy spectrum measured with the end-channel detector located along the beam axis 250 mm downstream of the secondary target. The production reaction is ^{1}H(^{17}O,^{17}F) n at a primary beam energy of 100 MeV and for a gas pressure of 950 mbar at room temperature. The voltage applied across the electrodes of the WF was $\pm$40 kV.

the maximum applicable voltage. In this case we can observe a nearly 100%-pure ^{17}F secondary beam.

Figure 3 shows the secondary beam energy spectrum measured with the end-channel silicon detector. This detector (active area, 48×48 mm^2; thickness, 500 μm) is placed along the beam axis 250 mm downstream the secondary target (see Fig. 1). This spectrum was obtained at the higher secondary beam energy after optimizing the magnetic fields of the second quadrupole triplet to increase the ^{17}F intensity. The purity of the secondary beam resulted as 93% and 96% at the lower and higher ^{17}F energies, respectively. The main contaminant was the ^{17}O^{8+} scattered beam with an energy $\sim$14 MeV smaller than that of ^{17}F.

D. Secondary beam tracking

The secondary beam spot on target was reconstructed event by event with the two x-y-position-sensitive PPACs (see Sec. II A). Figure 4 shows the horizontal (left column) and vertical (right column) ^{17}F-beam profiles measured with PPAC_A (top row) and PPAC_B (middle row). These spectra were collected placing a 15-mm-diameter hole at the position of the secondary target and requiring an "AND" condition between the cathodes of both PPACs and the end-channel detector. One can appreciate the 1-mm sensitivity of the PPAC coordinates, especially the horizontal coordinate of PPAC_A, and also the shadow induced by the 12-mm-diameter collimator located behind PPAC_B. An overall position resolution of about 1.3 mm was achieved for the target-position-reconstruction technique. The full widths at half maximum (FWHMs) of the ^{17}F-beam spot on target (bottom row of Fig. 4) were $\sim$8 and $\sim$9 mm in the horizontal and vertical planes, respectively, for both secondary beam energies. The reconstructed profiles are clearly compatible with the 15-mm-diameter hole located at the target position.

III. EXPERIMENT

Once a secondary beam intensity of $\sim$10^5 pps was achieved, the ^{17}F beam was sent onto a 1.0-mg/cm^2-thick
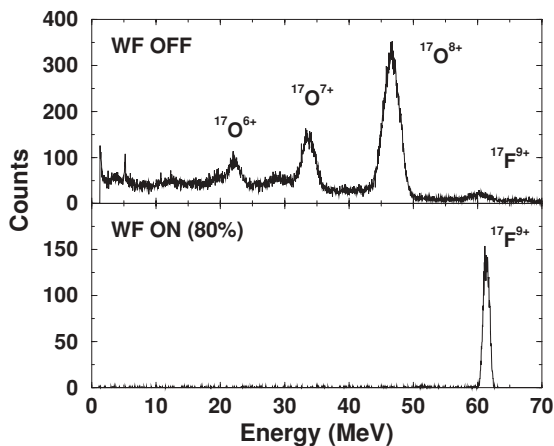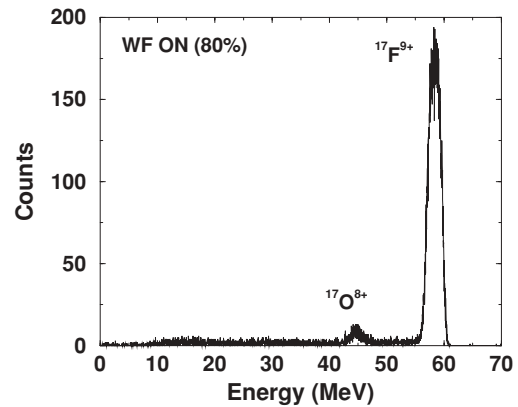

FIG. 2. Energy spectra collected with a silicon detector placed along the beam axis 700 mm upstream the secondary target. The production reaction is ^{1}H(^{17}O,^{17}F)n at a primary beam energy of 100 MeV and for a target gas pressure of 750 mbar at liquid-nitrogen temperature. The upper spectrum was obtained with the WF off, while the lower one was collected with a voltage difference $\pm$40 kV (corresponding to 80% of the maximum applicable voltage) across the WF electrodes.
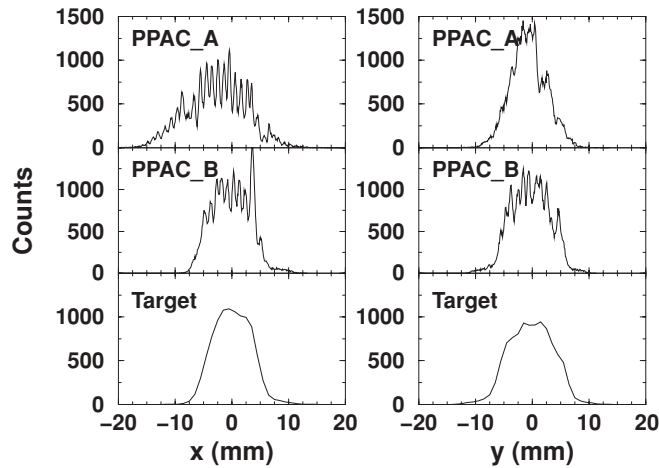
FIG. 4. ^{17}F horizontal (left column) and vertical (right column) secondary beam profiles. The top and middle rows were measured with the x-y-position-sensitive PPAC_A and PPAC_B, respectively. The bottom row corresponds to the event-by-event reconstruction of the secondary beam profile at the target position. The target profiles appear smoother because they were plotted with a 1-mm binning, whereas the original signals collected by the PPACs were used in the top and middle rows. See text for additional details.

self-supporting ^{58}Ni target. The data acquisition time was about 36 h at 54.1 MeV and 24 h at 58.5 MeV.

A. Experimental setup

Charged particles produced from the interaction of ^{17}F ions with a target ^{58}Ni were detected by means of the array EXODET [35]. This setup consists of eight $\Delta E - E_{\text{res}}$ silicon telescopes. The thickness of the ΔE layers ranges from 40 to 70 μm, while all E_{res} stages are 500 μm thick. The telescopes are arranged along the faces of two cubes closely packed around the target positions. In the present experiment the minimum distance between the target plane and the telescopes located at forward and backward angles was 7 and 13 mm, respectively. This configuration allowed for a $\sim$70% coverage of 4π sr.

Each EXODET detector has the front side segmented into 100 strips with a pitch size of 0.5 mm, while the back plane is a single pad. The strips of the $\Delta E(E_{\text{res}})$ stages are mounted orthogonally (parallel) to the beam axis. Such a configuration ensures a position accuracy of 0.5×0.5 mm^2 for particles passing through the inner layer. The energy signal is collected from the back plane of the detector and processed with standard electronics, while the position information is gathered from the segmented side and read by means of an ASIC chipset. The chip provides a data stream containing the number of hit strips and for each hit strip the following digital parameters: jitter time (JT) and time over threshold (ToT). The JT is the time interval between the arrival of a signal to the chip and the assertion of a valid trigger. It is a sort of time-correlation measurement. The ToT represents the time spent by any signal, after its amplification and shaping, above an externally settable threshold. Both JT and ToT are measured in units of a clock cycle with a frequency of 15 MHz, corresponding to a time resolution of $\sim$67 ns.
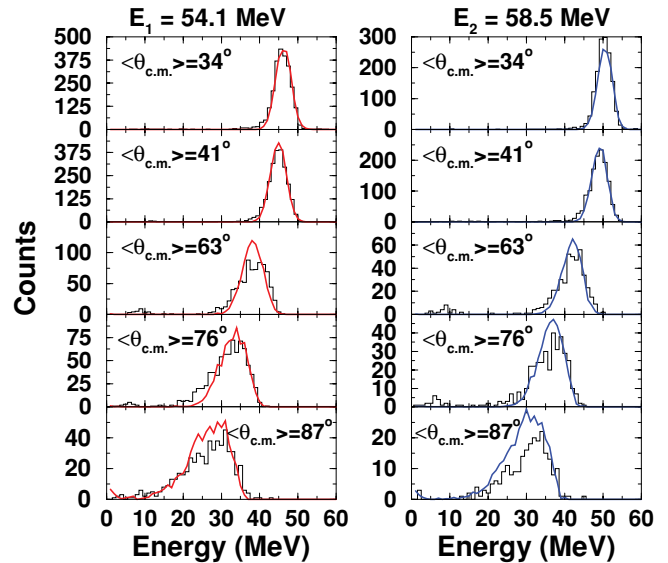

FIG. 5. (Color online) Charged reaction products energy spectra collected at forward angles for the interaction of ^{17}F ions with a ^{58}Ni target at two beam energies: 54.1 MeV (left column) and 58.5 MeV (right column). Experimental data are drawn with histograms, while continuous lines are the results of Monte Carlo calculations assuming a pure Rutherford scattering process. See text for additional details.

Because 40 μm of silicon is sufficient to stop completely ^{17}F and ^{16}O ions up to 61.7 and 53.2 MeV, respectively, ^{17}F scattered particles and ^{16}O reaction products in the energy range of our experiment were stopped in the first stage of EXODET. The data acquisition system was triggered by the "OR" of all the ΔE EXODET detectors in coincidence with cathode signals of PPAC_A "AND" PPAC_B. Trigger rates of about 5–7 Hz were typically recorded during the experiment.

B. Data analysis

Figure 5 shows the experimental energy spectra (histograms) for charged reaction products originated from the interaction of ^{17}F nuclei with the proton-shell closed target ^{58}Ni at 54.1 MeV (left column) and 58.5 MeV (right column) for average polar angles $\theta_{\text{c.m.}}$ from 34° (top row) to 87° (bottom row). For statistical purposes the data were grouped into bins of four to six strips. Each panel in Fig. 5 refers to one of these multistrips.

The JT digital information was used to provide a further selection condition on the experimental data. Figure 6 shows a typical JT spectrum collected at a ^{17}F incident energy of 54.1 MeV. One can clearly see that events within channels 5–6 had a good time correlation with the trigger. The ToT digital signal was not suited for the present analysis, because it did not provide the resolution needed to resolve $Z = 9$ (i.e., ^{17}F) from $Z = 8$ (i.e., ^{16}O) events and the sensitivity to $Z = 1$ reaction products was not enough owing to their small energy loss into the inner stage of EXODET ($\Delta E < 1.8$ MeV).

At very forward angles ($\theta_{\text{c.m.}} \sim 34°$) an overall experimental energy resolution of about 4.7 MeV was achieved, as can be seen from the top row in Fig. 5. Therefore, as we discuss in detail in Sec. IV, elastic scattering events could not be
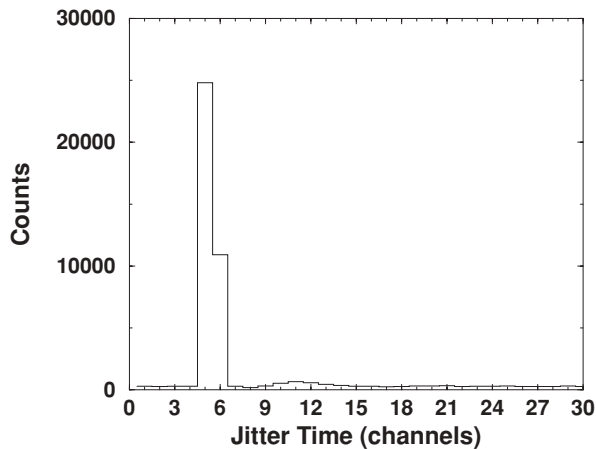
FIG. 6. JT spectrum collected from the EXODET modules located in the forward hemisphere for the reaction ^{17}F + ^{58}Ni at 54.1 MeV. Each channel corresponds to a time interval of about 67 ns.

FIG. 7. (Color online) Quasielastic differential cross sections for the system ^{17}F + ^{58}Ni at 54.1 and 58.5 MeV. Plotted errors include both statistical and systematical uncertainties. The solid and the dashed lines are the results of the optical model analysis performed according to the procedure described in detail in Sec. IV.

distinguished experimentally according to their energy deposit into the ΔE layer from (i) inelastic processes leading to the excitation of projectile and target low-lying states, (ii) transfer reaction products, and (iii) ^{16}O breakup fragments. Hereafter we globally refer to all these (experimentally undistinguishable) reaction channels as "quasielastic" processes.

Owing to the cubic and closely packed configuration of the detector array EXODET and to the rather large secondary beam spot on target, each ΔE strip covered a wide range of polar angles. This interval ranged from $5°$–$6°$ for the multistrips closest to the target position ($\langle\theta_{c.m.}\rangle \sim 87°$) to about $10°$ for the furthest multistrip from the target ($\langle\theta_{c.m.}\rangle \sim 34°$). To evaluate the overall efficiency of the experimental setup and to extract the quasielastic angular distribution, we developed an *ad hoc* Monte Carlo code. The code took into account: (i) the kinematics of the elastic scattering process, (ii) the Rutherford cross section, (iii) the geometry of the detector array EXODET, (iv) the secondary beam energy spread ($\sigma_E = 1.1$ and 1.0 MeV at the higher and lower energy, respectively, measured with the end-channel detector), (v) the secondary beam spot on target ($\sigma_x = 3.4$ mm and $\sigma_y = 3.8$ mm, reconstructed with the PPAC detectors as described in Sec. II D), (vi) the energy loss within the whole target thickness (evaluated with the code TRIM [36]), and (vii) the experimental energy resolution (3.5%–4.0%, measured with 5.485-MeV α particles).

In the simulation a random interaction point along the whole target thickness (1.12 μm) was assumed event by event and the kinetic energy of the incoming particle was decreased according to the distance covered inside the target. The results of the simulations are displayed with continuous lines and directly compared to the experimental data in Fig. 5. The normalization of the simulated data was performed by requiring that the integrated areas under the elastic peak corresponded to the experimental values at the most forward angles ($\theta_{c.m.} \leqslant 50°$), where the differential cross section is expected to be purely Rutherford at both secondary beam energies. Figure 7 shows differences up to 4.5% from the Rutherford behavior in the "normalization" range, which essentially reflect the accuracy of the Monte Carlo simulation.
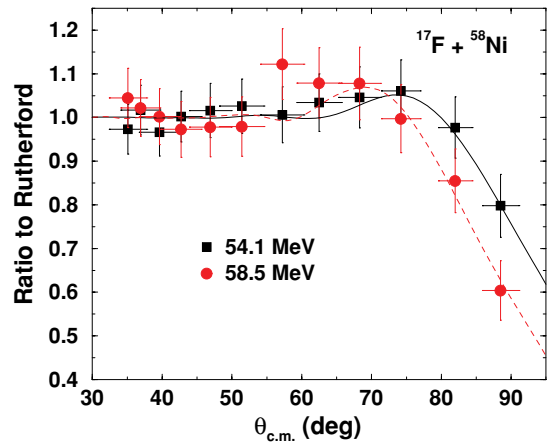
Substantial deviations from a pure Coulomb scattering process are clearly evident in the panels of Fig. 5 for $\theta_{c.m.} \geqslant 80°$ at 54.1 MeV and for $\theta_{c.m.} \geqslant 73°$ at 58.5 MeV. For each multistrip the value of the quasielastic differential cross section was determined from the ratio between the integrals of experimental and simulated data over the same energy range. The results are displayed in Fig. 7 for both secondary beam energies. The plotted data were obtained by averaging the angular distributions measured by each ΔE detector located in the forward hemisphere. The statistics collected from the detectors at backward angles was not sufficient to add any additional points to the angular distributions. Errors plotted in Fig. 7 include statistical fluctuations and a 5% systematical uncertainty owing to the accuracy of the Monte Carlo simulation, whereas the horizontal error bars account for the wide range of polar angles covered by each multistrip.

IV. THEORETICAL ANALYSIS

The collected data were analyzed within the framework of the optical model by means of the coupled-channel code FRESCO [37]. As already stated, owing to the limited energy resolution, pure elastic scattering events could not be distinguished from (i) inelastic scattering processes (see Sec. IV A), (ii) transfer channels (Sec. IV B), and (iii) breakup events ^{17}F $\rightarrow$ ^{16}O + p (Sec. IV C). The following paragraphs present the procedure adopted to describe these reaction channels and to include all of them simultaneously into the formalism of FRESCO.

A. Inelastic scattering

We considered inelastic excitations leading to the first (and only one bound) ^{17}F excited state ($E_x = 0.4935$ MeV, $J^\pi = 1/2^+$) and to the first ^{58}Ni excited state ($E_x = 1.454$ MeV, $J^\pi = 2^+$). We carried out, following the procedure described in Sec. III B, a Monte Carlo simulation also for these two inelastic scattering processes. Figure 8(a) shows that, for a test case at 54.1 MeV beam energy and for a multistrip around
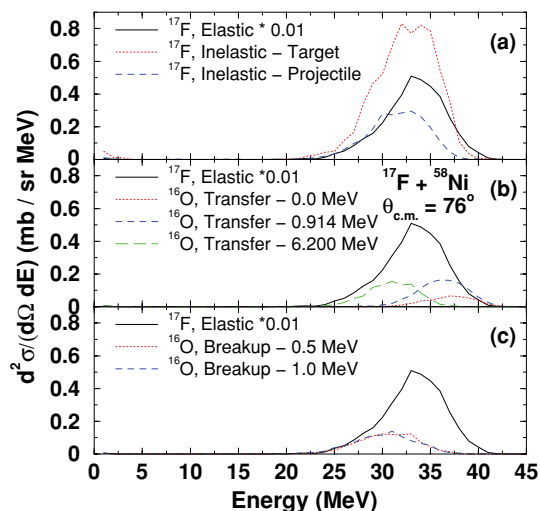
FIG. 8. (Color online) Calculated ^{17}F and ^{16}O energy spectra for inelastic scattering processes leading to the excitation of first excited state of ^{17}F and ^{58}Ni (a), for p stripping reactions leading to the ^{59}Cu ground state, second excited state (0.914 MeV), and a (possible) state with excitation energy around the Q_{opt} window (b), and for a breakup process occurring at excitation energies of 0.5 and 1.0 MeV above the breakup threshold (c). The calculated energy spectrum (multiplied by a factor of 0.01) for the ^{17}F elastic scattering process was added to each panel for comparison. The calculations were performed for a secondary beam energy of 54.1 MeV and for a multistrip around $\theta_{c.m.} = 76°$. For all processes but the elastic scattering, constant differential cross sections in the center-of-mass frame were employed for simplicity. More realistic angular distributions, for instance, peaked around the reaction grazing angle, would only slightly modify the shape of the spectra. The curves were normalized to the differential cross sections calculated at $\theta_{c.m.} = 76°$. For the transfer process to a ^{59}Cu excited state at 6.2 MeV, a differential cross section of 1.0 mb/sr was assumed.

$\theta_{c.m.} = 76°$, the expected energy ranges for both projectile and target excitations lie in the same energy interval of elastic scattering events. The curves in Fig. 8(a) were normalized to the differential cross sections computed at $\theta_{c.m.} = 76°$. Differences in shape between the energy spectra for elastic and inelastic processes are attributable to the fact that in the first case the events were generated according to the differential Rutherford cross section, whereas for simplicity flat distributions in the center-of-mass frame were entered for inelastic excitations. The use of more realistic angular distributions, for instance, peaked around the grazing angle of the reaction, would only imply a slightly modified shape of the energy spectra. Scattering events leading to target states at excitation energies higher than 1.4 MeV were not taken into consideration because their contributions are expected to be much smaller than that arising from the excitation of the ^{58}Ni first excited state.

Inelastic excitations were included into the calculations performed with the coupled-channel code FRESCO by means of their experimental transition probabilities: $B(E2 : 5/2^+ \rightarrow 1/2^+) = 21.64 \ e^2 \ \text{fm}^4$ [38] and $B(E2 : 0^+ \rightarrow 2^+) = 695 \ e^2 \ \text{fm}^4$ [39] for the projectile and target first excited state, respectively.

TABLE I. List of the transfer processes considered for the calculations performed with the coupled-channel code FRESCO. For each channel we indicated the ejectiles (second column), the ground-state-to-ground-state Q$_{value}$ (Q_{gg}, third column), the optimum Q$_{value}$ for both ^{17}F-beam energies (Q_{opt}, fourth column), and the final-state excitation energy ($E_x = Q_{gg} - Q_{opt}$, fifth column). Other stripping processes were not taken into account because they involve the rather unfavorable breaking of the ^{16}O core of ^{17}F.

Process	Ejectile	Q_{gg} (MeV)	Q_{opt} (MeV)	E_x (MeV)
p stripping	^{16}O	+2.82	−3.20/−3.47	+6.02/+6.29
n pickup	^{18}F	−3.07	≈0	−3.07
α pickup	^{21}Na	+0.16	+5.42/+5.90	−5.26/−5.74
t pickup	^{20}Ne	+2.79	+2.87/+3.12	−0.08/−0.33
$2n$ pickup	^{19}F	−2.88	≈0	−2.88

B. Transfer channels

The possibility that transfer channels could be populated in this energy range was also investigated within the coupled-channel formalism. In particular, we considered the processes listed in Table I. According to the semiclassical model of Brink [40], transfer channels should preferably populate final states with excitation energies around $E_x = Q_{gg} - Q_{opt}$, Q_{gg} being the ground-state-to-ground-state Q_{value} and Q_{opt} the optimum Q_{value}, defined by the formula

$$Q_{opt} = \left(\frac{Z_b Z_B}{Z_a Z_A} - 1 \right) E_{c.m.}, \tag{1}$$

where Z_a and Z_A are the atomic numbers of the two particles in the initial state, Z_b and Z_B those of the two particles in the final state, and $E_{c.m.}$ the bombarding energy in the center-of-mass frame. Table I shows that E_x is negative for all the considered pickup reactions, while the population of excited states at excitation energies $E_x \approx 6.0$–6.3 MeV is expected for the p stripping channel. Therefore, contributions arising from pickup processes should be presumably negligible with respect to that of the p stripping and in the following calculations we considered only this transfer channel.

1. p stripping

We included into the coupled-channel calculations p stripping channels leading to the ^{16}O ground state and to the following ^{59}Cu levels: ground state ($E_x = 0$ MeV, $J^\pi = 3/2^-$), first excited state ($E_x = 0.491$ MeV, $J^\pi = 1/2^-$), and second excited state ($E_x = 0.914$ MeV, $J^\pi = 5/2^-$). These three states could be nicely described as single-particle excitations of the targetlike particle, with the last proton orbiting in a $2p_{3/2}$, $2p_{1/2}$, and $1f_{5/2}$ shell, respectively, around the ^{58}Ni core and they were all entered into the calculations of FRESCO with spectroscopic factors equal to 1. At excitation energies higher than 1.4 MeV, the level scheme of ^{59}Cu becomes rather complicated owing to the presence of several particle-hole and core excitations, for which a description in terms of single-particle excitations is not possible. Thus, the highest ^{59}Cu excited state included into the theoretical calculations is still 5 MeV below the Q_{opt} window, where the largest contributions are expected. The situation is further

complicated by the fact that this region lies above the ^{59}Cu proton separation threshold ($S_p = 3.4185$ MeV). Finally, we noticed that only transfer channels to negative parity states were included, whereas considerable contributions from transfers to positive-parity states are also expected.

The ^{16}O simulated energy ranges for transfer channels leading to the ^{59}Cu ground state, to the excited state at $E_x = 0.914$ MeV, and to a (possible) level with an excitation energy $E_x = 6.2$ MeV are shown in Fig. 8(b). Also in this case, the spectra were computed using for simplicity a flat angular distribution in the center-of-mass frame and were normalized to the differential cross sections calculated at $\theta_{c.m.} = 76°$. For the transfer process to a ^{59}Cu excited state at $E_x = 6.2$ MeV a differential cross section of 1.0 mb/sr was assumed. We could see that for processes leading to ^{59}Cu low-lying states the maxima of the energy spectra are located 3–4 MeV at the right side with respect to the top of the curve related to the ^{17}F elastic scattering process. However, both distributions have FWHMs of about 6–7 MeV and they nearly overlap for the whole energy interval. Moreover, the intensity of the elastic scattering process in the angular range covered by our experimental setup is expected to be two orders of magnitude larger than transfer channels. The situation is even more severe for p stripping processes around the Q_{opt} window because in this case the ^{16}O expected energy range lies exactly below the low-energy side of the elastic peak.

C. Breakup process

Owing to its very small binding energy ($S_p = 0.600$ MeV), there is rather a large probability that the ^{17}F projectile could break into the pair ^{16}O + p in the proximity of the Coulomb and nuclear fields of a ^{58}Ni target. Monte Carlo simulations carried out for ^{17}F excitation energies 0.5–1.0 MeV above the proton separation energy [see Fig. 8(c)] show that the ^{16}O expected energy ranges lie below the low-energy tail of the elastic peak. Therefore, also ^{16}O ions originated from the breakup process could not be distinguished experimentally from elastic scattering events. Breakup protons could also not be unambiguously detected via the $\Delta E - E_{res}$ technique owing to the very small thickness of the inner stage of EXODET, as already stated in Sec. III B (see also Refs. [30,31]). Furthermore, according to the breakup kinematics and for an excitation energy 1 MeV above the breakup threshold, protons would be produced with a rather large (2 MeV FWHM) energy distribution centered around 3.5 MeV, which would make in most cases even the energy deposit into the E_{res} too small to be efficiently processed by the chip ASIC.

In our theoretical framework, the breakup process for the reaction ^{17}F + ^{58}Ni was described according to a single-particle model [41,42], where the bound $1d_{5/2}$ valence proton in ^{17}F, moving with respect to the ^{16}O core, is promoted to continuum states. The parameters of the proton-core Woods-Saxon and spin-orbit potentials were adjusted to simultaneously reproduce energies and root mean square radii (as given in Ref. [43]) for both projectile bound states. This was obtained with a spin-orbit potential larger than usual that deepens the potential well at the surface, giving bound wave function with a more pronounced halo character and consequently larger
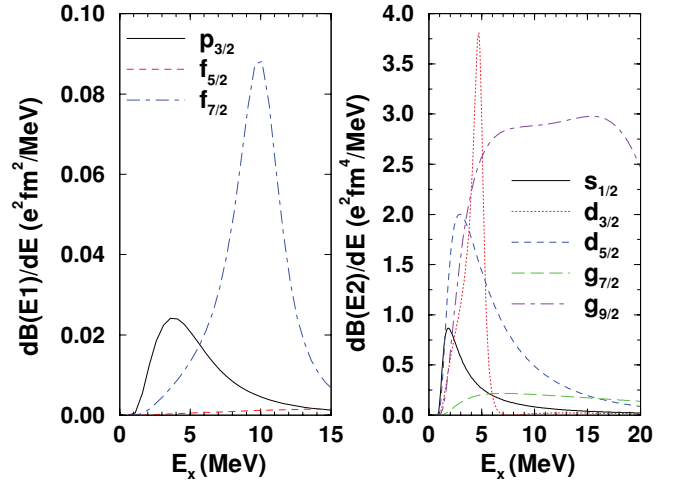

FIG. 9. (Color online) Differential transition rates to the continuum for dipole (left) and quadrupole (right) electric operators. The initial state is the $d_{5/2}$ ground state of ^{17}F, and the final states are continuum states of the ^{16}O + p system with quantum numbers indicated in the legend. The quadrupole response shows the combined effect of resonant and nonresonant behavior for some multipolarities, while this is absent in the dipole response.

root-mean-square radii. In addition, a $B(E2)$ from the $1d_{5/2}$ ground state to the first excited $2s_{1/2}$ state of 19.8 e^2 fm^4 was obtained, which compares reasonably well with the measured value of 21.64 e^2 fm^4 [38]. The same Woods-Saxon plus spin-orbit potential was retained for the continuum, giving, for instance, a $1d_{3/2}$ resonance about 4–5 MeV above the threshold, in fair accordance with the observed resonances just above $E_x = 5$ MeV (see Fig. 9). The bound state and continuum wave functions were used to calculate the electromagnetic response to the continuum, including $E1$ (to $p_{3/2}$, $f_{5/2}$, $f_{7/2}$) and $E2$ (to $s_{1/2}$, $d_{3/2}$, $d_{5/2}$, $g_{7/2}$, $g_{9/2}$) transitions. Magnetic and higher-order electric transitions were neglected because they are presumably quite small.

To include the breakup process into our calculations, the continuum above the breakup threshold was discretized into 254 bins. For dipole excitations, 0.5-MeV bins up to $E_x = 14.1$ MeV were considered, whereas 0.3-MeV bins up to $E_x = 10.6$ MeV were used for quadrupole excitations. For each bin a transition probability $B(E\lambda)$ equal to the integral over the bin width of the transition rates depicted in Fig. 9 was employed.

D. Optical model calculations

The interaction potential between ^{17}F and ^{58}Ni used as starting point for the optical model analysis was described according to a standard Akyüz-Winther [44] parametrization. The real part was a Woods-Saxon well with the following parameters: $V_0 = 52.24$ MeV, $r_0 = 1.18$ fm, and $a_0 = 0.63$ fm. For the imaginary part of the potential we also assumed a Woods-Saxon well with $W_0 = V_0/2$, $r_i = r_0$, and $a_i = a_0$.

We searched for the best fit of the experimental data displayed in Fig. 7, with the sum of the angular distributions for the elastic process, the inelastic excitations to the first projectile and target excited states, the breakup channel, and p stripping processes leading to the already mentioned three

states of ^{59}Cu. All these mechanisms were simultaneously included into the coupled-channel code FRESCO according to the formalism described in Secs. IV A–IV C. The fits were then performed fixing both radii and both diffusenesses to the initial values, while the real and imaginary depths of the potential were left free to vary. To account for the rather large energy lost by the ^{17}F secondary beam into the target ($\Delta E \approx 4.3$ MeV, estimated with the code TRIM [36]), we divided the target thickness into three 0.333-mg/cm^2-thick bins and we computed the ^{17}F reaction energy at the middle position of each "subtarget." These energies were 53.4, 52.0, and 50.5 MeV and 57.8, 56.5, and 55.1 MeV for the lower and higher secondary beam energies, respectively. We then fitted each experimental data set at three different bombarding energies and from each fit we extracted the optical model best-fit parameters, the reaction cross section, and the cross sections for the quasielastic processes included into the coupled-channel analysis. Small variations ($\leqslant 5\%$) between different subtargets were observed for the reaction cross sections, and moderate fluctuations (up to 12%–15%) were noticed for the estimates of the cross sections for inelastic excitations and for the breakup process, whereas the strongest dependence on the reaction energy (up to 46%–60%) was shown by the p stripping cross sections. This outcome pointed out already somewhat the limits in the description of this transfer reaction mechanism within our theoretical approach. Table II lists for both secondary beam energies the optical model parameters related to the middle subtarget and the cross sections obtained by averaging the values individually obtained for the three target bins.

Figure 10 shows the overall results of the fitting procedure in the angular range $\theta_{\text{c.m.}} = 40°$–$95°$, where we highlighted the contributions of different reaction mechanisms at both secondary beam energies. In particular, we can see that at $\theta_{\text{c.m.}} = 76°$ inelastic excitations represent $\sim 2.4\%$–2.5% of
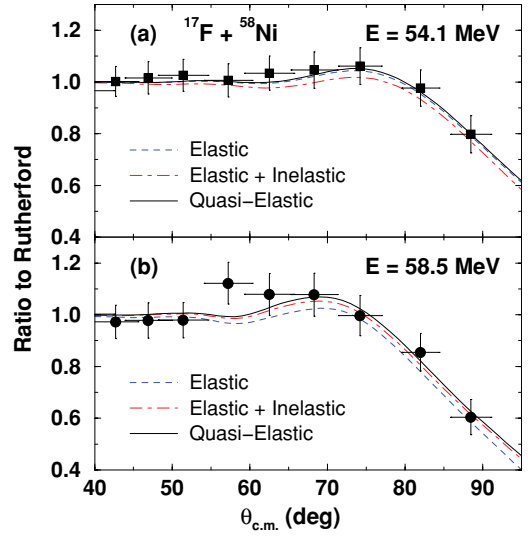

FIG. 10. (Color online) Optical model analysis of the experimental quasielastic angular distributions for the system ^{17}F + ^{58}Ni at 54.1 (a) and 58.5 (b) MeV secondary beam energy. Dashed, dot-dashed, and solid lines show the contribution of the elastic scattering process ("Elastic"), the sum of the elastic and inelastic scattering angular distributions ("Elastic + Inelastic"), and the sum of differential cross sections for the elastic, inelastic, p stripping, and breakup processes ("Quasi-Elastic"), respectively.

the elastic scattering angular distributions, while transfer and breakup channels account globally for $\sim 0.8\%$–1.7%.

Table II shows that the cross sections for transfer channels increase with the excitation energy of the populated ^{59}Cu excited state. Because the semiclassical model of Brink predicts that the largest cross sections should arise for states with $E_x \approx 6.0$–6.3 MeV, the values we computed have to be considered as lower limits for the cross section of the (whole) p stripping process. In addition, we noticed that, while the cross sections for inelastic excitations and for the breakup channel increase (on average) by 10% and 28%, respectively, from the lower to the higher beam energy, the cross sections for transfer processes are more than a factor of two larger at 58.5 MeV with respect to those at 54.1 MeV. This feature suggests that the quasielastic data at the secondary beam higher energy could be more "contaminated" from transfer channels than those at the lower energy. This fact could influence in turn the reaction cross section, which increases only by 10% between the two energies, whereas "scaled" reaction cross-section data for the system ^{16}O + ^{58}Ni [45] increases by 55% over the same energy range.

The comparison with the system ^{16}O + ^{58}Ni also showed that direct reaction channels other than the elastic scattering are more relevant for the reaction induced from the loosely bound projectile ^{17}F. In fact, according to the analysis performed in [45], in the energy range of our experiment, quasielastic channels accounts for 11%–12% of the whole reaction cross section for the system ^{16}O + ^{58}Ni, whereas in our case the sum of inelastic scattering, transfer, and breakup processes covers at least 17%–19% of the reaction cross section. This outcome is a clear signature of the key role played in the reaction dynamics

TABLE II. Optical model parameters, reaction cross sections (σ_R) and cross sections for the excitation of the projectile ($\sigma_{\text{Inel,Proj.}}$) and target ($\sigma_{\text{Inel,Tar.}}$) first excited states, for the breakup process (σ_{Breakup}), for the p stripping transfer leading to the ^{59}Cu ground state ($\sigma_{p\text{-str,g.s.}}$), first ($\sigma_{p\text{-str,1st ex.s.}}$) and second ($\sigma_{p\text{-str,2nd ex.s.}}$) excited states. The values refer to the best-fits of the experimental data at the lower (second column) and higher (third column) ^{17}F secondary beam energy. All fits were performed with $r_0 = r_i = 1.18$ fm and $a_0 = a_w = 0.63$ fm. The optical model parameters are related to the middle sub-target, while the cross sections were obtained by averaging the values individually obtained for different subtargets. See text for additional details.

	$E = 54.1 \pm 1.1$ MeV	$E = 58.5 \pm 1.0$ MeV
V_0	56.7 ± 15.7 MeV	28.0 ± 7.8 MeV
W_0	24.4 ± 5.1 MeV	12.1 ± 3.7 MeV
σ_R	510.5 ± 55.3 mb	559.7 ± 64.3 mb
$\sigma_{\text{Inel,Proj.}}$	20.5 ± 1.1 mb	22.1 ± 1.3 mb
$\sigma_{\text{Inel,Tar.}}$	46.4 ± 2.2 mb	52.6 ± 2.9 mb
σ_{Breakup}	11.1 ± 0.7 mb	14.2 ± 0.9 mb
$\sigma_{p\text{-str,g.s.}}$	1.5 ± 0.2 mb	4.0 ± 0.6 mb
$\sigma_{p\text{-str,1st ex.s.}}$	1.8 ± 0.2 mb	4.2 ± 0.6 mb
$\sigma_{p\text{-str,2nd ex.s.}}$	3.9 ± 0.7 mb	9.3 ± 2.0 mb

TABLE III. Calculated cross sections for p stripping processes leading to ^{59}Cu positive-parity states in the excitation energy range $E_x = 1.0$–3.4 MeV. Data in second (third) column refer to the lower (higher) ^{17}F secondary beam energy.

	$E = 54.1$ MeV	$E = 58.5$ MeV
$2d_{5/2}$	4.6–16.2 mb	8.8–24.8 mb
$3s_{1/2}$	2.2–12.4 mb	4.1–17.6 mb
$2d_{3/2}$	6.0–21.4 mb	10.7–30.9 mb

at near-barrier energies by the low binding energy of the ^{17}F valence proton.

We finally performed explorative calculations to estimate possible contributions arising from p stripping processes leading to ^{59}Cu positive-parity states. For this purpose we added to the input of FRESCO three ^{59}Cu excited states with energy variable in the range $E_x = 1.0$–3.4 MeV, with spectroscopic factors equal to 1 and with the quantum numbers of the following shell model orbits: $2d_{5/2}$, $3s_{1/2}$, and $2d_{3/2}$. These calculations, summarized in Table III, are only indicative because these "pure" single-particle states are actually split into several states by the residual interaction. For all states, we observed increasing cross sections with increasing excitation energies and especially large contributions from d states, which correspond to $\Delta l = 0$ transfers. Considering that the $Q_{\rm opt}$ window is still 3 MeV above the highest excitation energies included in the calculations, it would not be surprising if the p stripping process would totally account for a cross section of even 50–100 mb, which would in turn increase the reaction cross section by approximately the same amount. This issue obviously needs to be verified experimentally.

V. DISCUSSION

The experimental data collected for the system ^{17}F + ^{58}Ni and their theoretical analysis within the framework of the optical model evidenced the relevance of direct reaction channels in the reaction dynamics induced from weakly bound nuclei at near-barrier energies.

In the present experiment, projectile and target inelastic excitations, transfer channels, and breakup events could not be separated from the pure elastic scattering channel. For inelastic excitations this problem is rather unavoidable, especially for the projectile excitation, owing to the poor emittance and limited energy resolution of in-flight secondary beams and to the large target thickness needed to compensate the RIB low intensity. On the contrary, the $\Delta E - E_{\rm res}$ technique, using very thin ($<20\ \mu$m) ΔE silicon detectors or ionization chambers, could be employed to unambiguously distinguish different elements and separate at least p stripping and breakup reaction products from elastic and/or inelastic scattering events.

In the theoretical analysis, we explicitly included inelastic excitations to the first excited state of both projectile and target, the breakup channel ^{17}F $\rightarrow$ ^{16}O + p, and p stripping channels to the ground state and to the first and second excited states of ^{59}Cu. The situation is rather under control for the inelastic channels, which contribute for 67–74 mb to the reaction cross sections and only weakly depend on the incoming energy.

Similar considerations can also be drawn for the breakup process, even if in this case the cross section exhibits a slightly steeper dependence on the secondary beam energy. However, the cross sections for the p stripping process are only indicative of the relevance of this reaction mechanism because excited states at excitation energies $E_x \approx 6$ MeV are expected to be populated with the largest probability, while our calculations stopped at $E_x < 1.0$ MeV. Therefore, the computed values of 7–15 mb should be considered as lower estimates of the cross section for this channel. Explorative calculations indicated that p stripping processes leading to ^{59}Cu positive-parity excited states in the range $E_x = 1.0$–3.4 MeV could have a cross section of 50–75 mb. Additionally, we noticed that the cross sections for the considered p stripping channels increase by a factor of two from the lower to higher energy of our experiment. Therefore, at the level of accuracy of our data it is not possible to establish the actual contribution of p stripping processes to the quasielastic data.

Figure 11 presents the "reduced" reaction cross sections deduced from elastic scattering measurements for six light projectiles interacting with a medium-mass target, ^{58}Ni or ^{64}Zn. The reduction was performed according to the procedure described in Ref. [46] to account for the different geometrical sizes of the colliding nuclei and the different Coulomb barrier heights. Following the outcomes of the explorative calculations performed for the p stripping process, 50 and 75 mb were quadratically added to the errors listed in Table II for the reaction cross-section data of the system ^{17}F + ^{58}Ni at the lower and higher secondary beam energy, respectively. We clearly see that at sub-barrier energies the "reduced" reaction cross sections for the p-halo and very loosely bound ^{8}B ($S_p = 0.138$ MeV) [47] and for the $2n$-halo ^{6}He ($S_{2n} = 0.975$ MeV) [16] are enhanced by even more than one order of magnitude with respect to the benchmark reaction induced from the very well bound ^{16}O isotope on a ^{58}Ni target [45]. This enhancement decreases, consistently with the projectile binding energy, to about a factor of 7–8 (at reduced energies around 0.9)
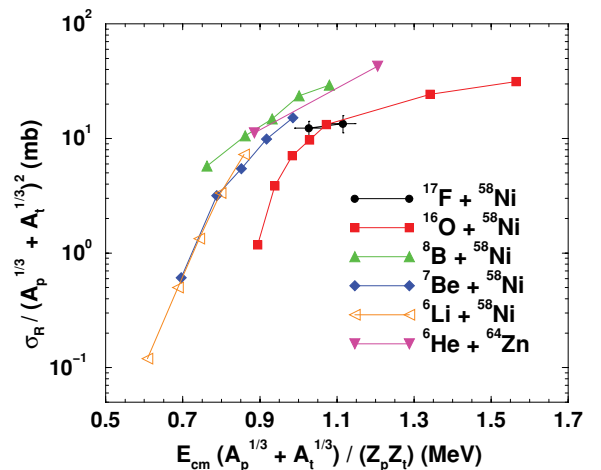

FIG. 11. (Color online) "Reduced" reaction cross sections for systems consisting of light projectiles interacting with a ^{58}Ni or ^{64}Zn target. The reduction is done according to the procedure described in Ref. [46].

and then down to a factor of 2–4 (at near-barrier energies) for the reactions induced from the more tightly bound ^{6}Li ($S_\alpha = 1.474$ MeV) and ^{7}Be ($S_\alpha = 1.586$ MeV) [47]. The present measurement for the system ^{17}F + ^{58}Ni suggests a 20% enhancement of the reaction cross section at the lower secondary beam energy, while the value at the higher energy is nearly superimposed to the curve for the system ^{16}O + ^{58}Ni.

VI. CONCLUSIONS

The scattering process of the ^{17}F RIB from the proton-shell closed ^{58}Ni target was investigated at two colliding energies slightly above the Coulomb barrier. The collected data were analyzed within the framework of the optical model by means of the coupled-channel code FRESCO. Because inelastic scattering events, transfer processes, and the breakup channel could not be distinguished experimentally from pure elastic scattering events, we included into the fitting procedure of the collected data the excitations to the first excited states of ^{17}F and ^{58}Ni, the p stripping transfers leading to the ground state and to first and second excited states of ^{59}Cu, and dipole and quadrupole excitations to the continuum above the ^{17}F breakup threshold up to $E_x = 14.1$ MeV and $E_x = 10.6$ MeV, respectively. We also investigated possible (strong) contributions arising from p stripping transfers leading to ^{59}Cu positive-parity states in the energy range $E_x = 1.0$–3.4 MeV. As a result of our analysis, at the lower energy, the "reduced" reaction cross section showed a rather moderate enhancement ($\sim$20%) with respect to the reference system ^{16}O + ^{58}Ni, while no enhancement has been observed at the higher secondary beam energy. This different behavior could be probably ascribed to the different degree of contamination from nonelastic channels of the two data sets because the relevance of these processes, especially of the p stripping (which we are not able to predict theoretically), increases with the bombarding energy. The performed analysis showed also that these channels are more strongly populated and thus provide a larger contribution to the reaction cross section than for the system ^{16}O + ^{58}Ni. This feature could probably be directly related to the low binding energy of the ^{17}F valence proton; however, further accurate experiments are needed to shed more light on this topic.

Future measurements should foresee not only the possibility of unambiguously distinguishing between ^{17}F and ^{16}O, but should also allow for the coincidence detection of ^{16}O ions and protons. The reconstruction of the Q_{value} spectrum of these events together with the angular correlations of the two particles (as recently done for reactions induced from the weakly bound stable projectile ^{9}Be [48]) will help to establish whether the enhancement of the reaction cross section with respect to the benchmark reaction ^{16}O + ^{58}Ni is mainly triggered from a transfer reaction (as observed for the 2n-halo ^{6}He [16–18,22–24] and for the 1n-halo ^{11}Be [49–51]) or from a breakup process (as indicated from first measurements performed with the 1p-halo ^{8}B [47]).

[1] M. Dasgupta, D. J. Hinde, N. Rowley, and A. M. Stefanini, Annu. Rev. Nucl. Part. Sci. **48**, 401 (1998) , and references therein.

[2] J. F. Liang and C. Signorini, Int. J. Mod. Phys. E **14**, 1121 (2005).

[3] L. F. Canto, P. R. S. Gomes, R. Donangelo, and M. S. Hussein, Phys. Rep. **424**, 1 (2006).

[4] N. Keeley *et al.*, Prog. Part. Nucl. Phys. **59**, 579 (2007).

[5] N. Keeley *et al.*, Prog. Part. Nucl. Phys. **63**, 396 (2009).

[6] M. Mazzocco, Int. J. Mod. Phys. E **19**, 977 (2010).

[7] K. Hagino, A. Vitturi, C. H. Dasso, and S. M. Lenzi, Phys. Rev. C **61**, 037602 (2000).

[8] M. Dasgupta *et al.*, Phys. Rev. C **70**, 024606 (2004).

[9] L. R. Gasques, D. J. Hinde, M. Dasgupta, A. Mukherjee, and R. G. Thomas, Phys. Rev. C **79**, 034605 (2009).

[10] R. J. Woolliscroft *et al.*, Phys. Rev. C **68**, 014611 (2003).

[11] C. Signorini *et al.*, in *Proceedings of the International Conference BO2000, Bologna, Italy, May 2000*, edited by D. Vretenar *et al.* (World Scientific, Singapore, 2001), p. 413.

[12] A. Pakou *et al.*, Phys. Rev. Lett. **90**, 202701 (2003).

[13] A. Pakou *et al.*, Phys. Rev. C **71**, 064602 (2005).

[14] C. Signorini *et al.*, Eur. Phys. J. A **10**, 249 (2001).

[15] C. Signorini *et al.*, Phys. Rev. C **67**, 044607 (2003).

[16] A. Di Pietro *et al.*, Phys. Rev. C **69**, 044613 (2004).

[17] A. Navin *et al.*, Phys. Rev. C **70**, 044601 (2004).

[18] A. Chatterjee *et al.*, Phys. Rev. Lett. **101**, 032701 (2008).

[19] D. Escrig *et al.*, Nucl. Phys. A **792**, 2 (2007).

[20] E. F. Aguilera *et al.*, Phys. Rev. Lett. **84**, 5058 (2000).

[21] E. F. Aguilera *et al.*, Phys. Rev. C **63**, 061603 (2001).

[22] R. Raabe *et al.*, Nature (London) **431**, 823 (2004).

[23] J. P. Bychowski *et al.*, Phys. Lett. B **596**, 26 (2004).

[24] P. A. De Young *et al.*, Phys. Rev. C **71**, 051601(R) (2005).

[25] J. J. Kolata *et al.*, Phys. Rev. C **75**, 031302(R) (2007).

[26] A. Pakou *et al.*, J. Phys. G **31**, S1723 (2005).

[27] K. E. Rehm *et al.*, Phys. Rev. Lett. **81**, 3341 (1998).

[28] J. F. Liang *et al.*, Phys. Rev. C **67**, 044603 (2003).

[29] M. Romoli *et al.*, Phys. Rev. C **69**, 064614 (2004).

[30] D. Pierroutsakou *et al.*, Eur. Phys. J. Special Topics **150**, 47 (2007).

[31] C. Signorini *et al.*, Eur. Phys. J. A **44**, 63 (2010).

[32] M. Mazzocco *et al.*, Nucl. Phys. A **834**, 488c (2010).

[33] F. Farinon *et al.*, Nucl. Instrum. Methods Phys. Res. B **266**, 4097 (2008).

[34] M. Mazzocco *et al.*, Nucl. Instrum. Methods Phys. Res. B **266**, 4665 (2008).

[35] M. Romoli *et al.*, IEEE Trans. Nucl. Sci. **52**, 1860 (2005).

[36] J. F. Ziegler *et al.*, *The Stopping and Range of Ions in Solids* (Pergamon Press, Oxford, 1984), Vol. 1.

[37] I. J. Thompson, Comput. Phys. Rep. **7**, 167 (1988).

[38] D. R. Tilley *et al.*, Nucl. Phys. A **564**, 1 (1993).

[39] S. Raman *et al.*, At. Data Nucl. Data Tables **78**, 1 (2001).

[40] D. M. Brink, Pyhs. Lett. B **40**, 37 (1972).

[41] L. Fortunato and A. Vitturi, Eur. Phys. J. A **26**, 33 (2005).

[42] A. Mason *et al.*, Eur. Phys. J. A **39**, 107 (2009).

[43] R. Morlock *et al.*, Phys. Rev. Lett. **79**, 3837 (1997).

[44] R. Broglia and A. Winther, *Heavy Ion Reactions* (Addison-Wesley, Reading, MA, 1990), p. 113.

[45] N. Keeley *et al.*, Nucl. Phys. A **582**, 314 (1995).

[46] P. R. S. Gomes, J. Lubian, I. Padron, and R. M. Anjos, Phys. Rev. C **71**, 017601 (2005).

[47] E. Aguilera *et al.*, Phys. Rev. C **79**, 021601(R) (2009).

[48] R. Rafiei, R. duRietz, D. H. Luong, D. J. Hinde, M. Dasgupta, M. Evers, and A. Diaz-Torres, Phys. Rev. C **81**, 024601 (2010).

[49] L. Acosta *et al.*, Eur. Phys. J. A **42**, 461 (2009).

[50] A. Di Pietro, Nucl. Phys. A **834**, 408c (2010).

[51] A. Di Pietro *et al.*, Phys. Rev. Lett. **105**, 022701 (2010).